Supporting Information

Integrated temperature and pressure dual-mode sensors based on elastic PDMS foams decorated with thermoelectric PEDOT:PSS and carbon nanotubes for human energy harvesting and electronic-skin

Fu-Lin Gao,[a] Peng Min,[b] Xuan-Zhi Gao,[a] Changjun Li,[a] Tingting Zhang,[a] Zhong-Zhen Yu,[b*] Xiaofeng Li[a*]

[a] State Key Laboratory of Organic-Inorganic Composites, College of Materials Science and Engineering, Beijing University of Chemical Technology, Beijing 100029, China

[b] Beijing Key Laboratory of Advanced Functional Polymer Composites, Beijing University of Chemical Technology, Beijing 100029, China

*E-mail: xfli@mail.buct.edu.cn (X. Li); yuzz@mail.buct.edu.cn (Z.-Z. Yu)

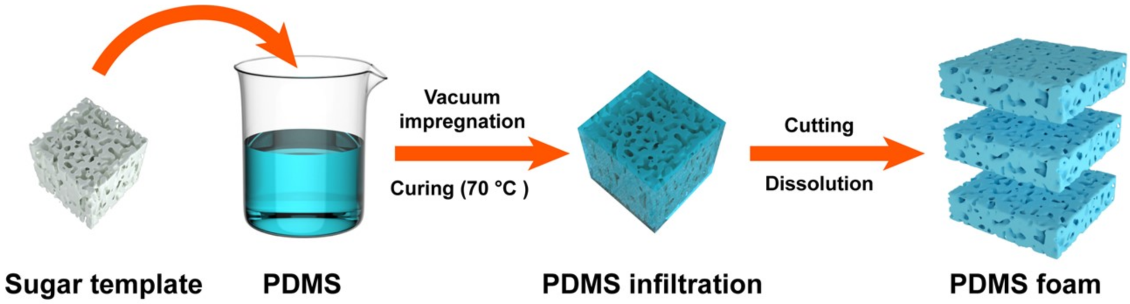

Figure S1. Preparation of PDMS foam by a sugar-template etching method.

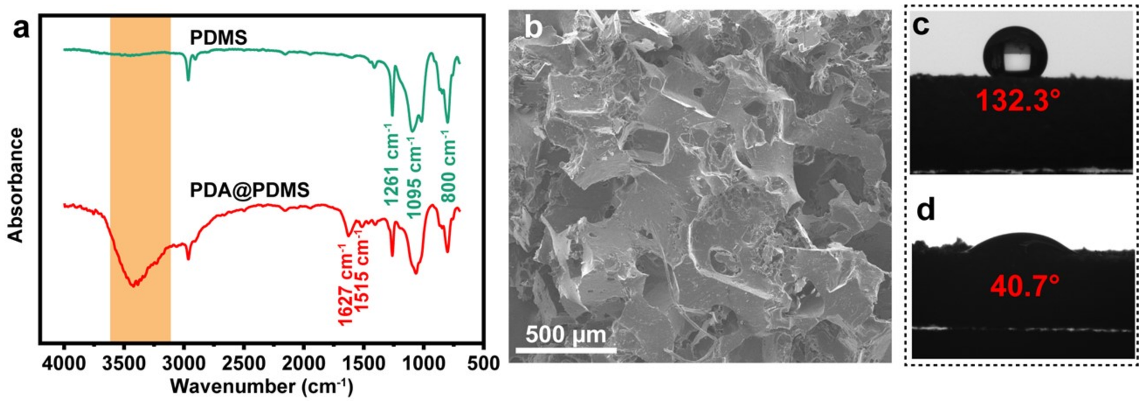

Figure S2. (a) FTIR spectra of pure PDMS and PDA@PDMS. (b) SEM image of pure PDMS foam. Water contact angle images of (c) pure PDMS foam, and (d) PDA@PDMS foam.

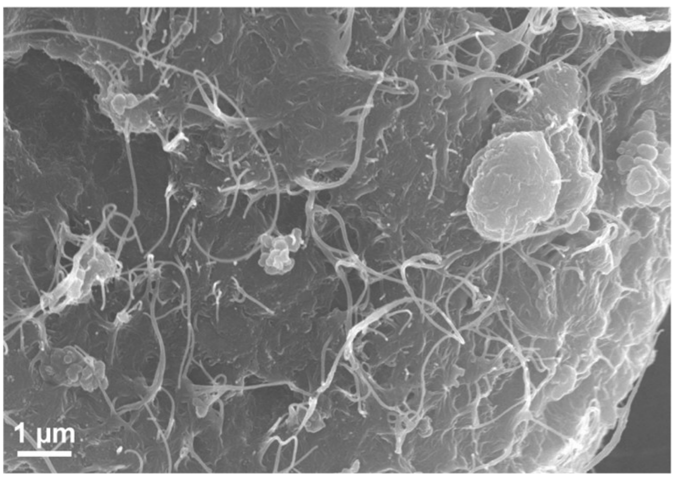

Figure S3. SEM image of the PCPP foam with CNT fraction of 100 wt%.

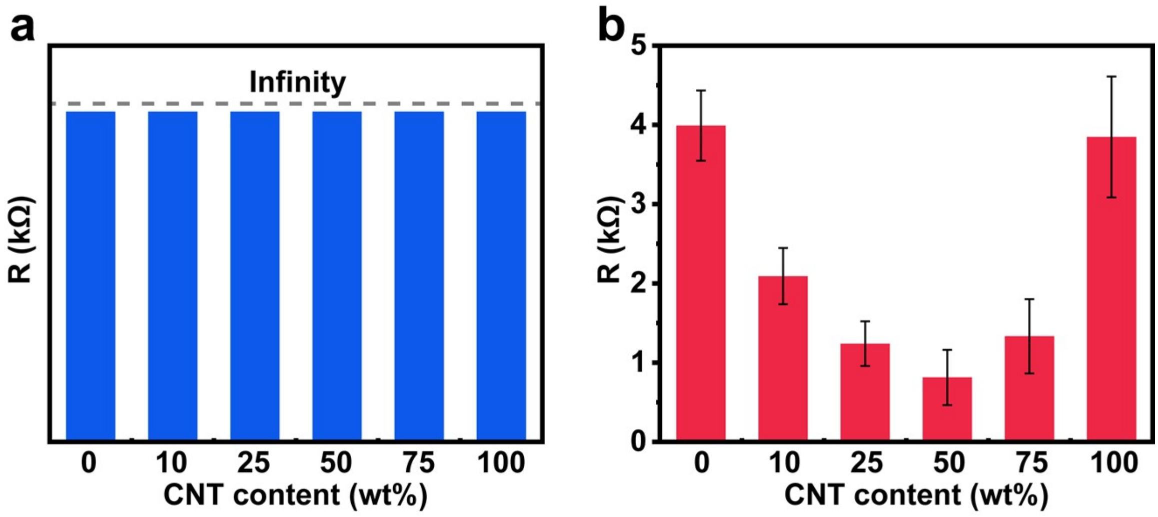

Figure S4. Electrical resistances of (a) PEDOT:PSS/CNT@PDMS foams and (b) PCPP foams with different CNT contents.

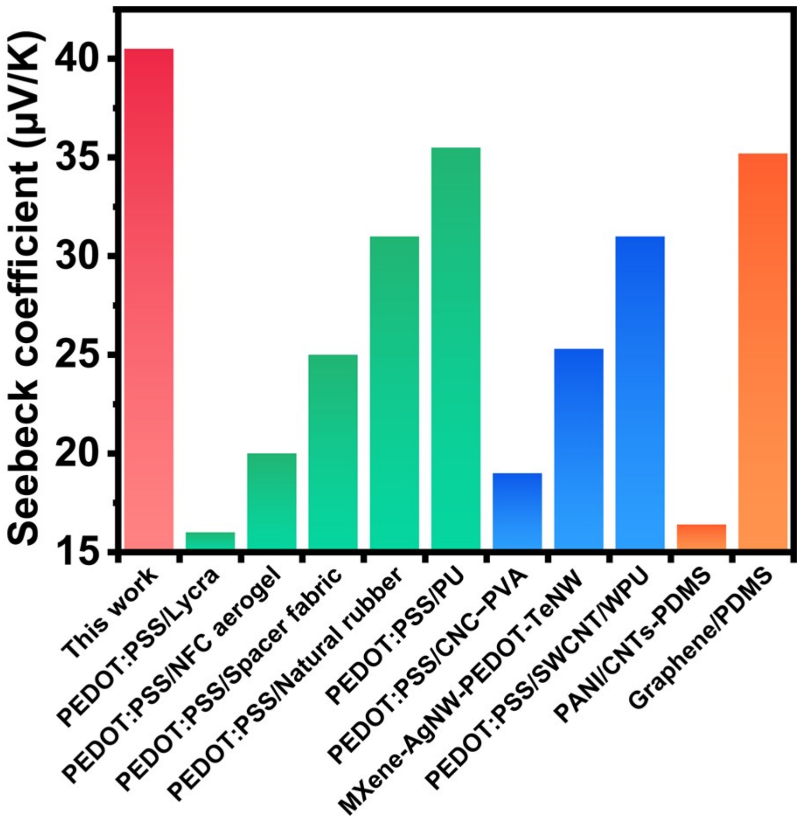

Figure S5. Comparison of the Seebeck coefficient of this work with those reported in the literature.[1-10]

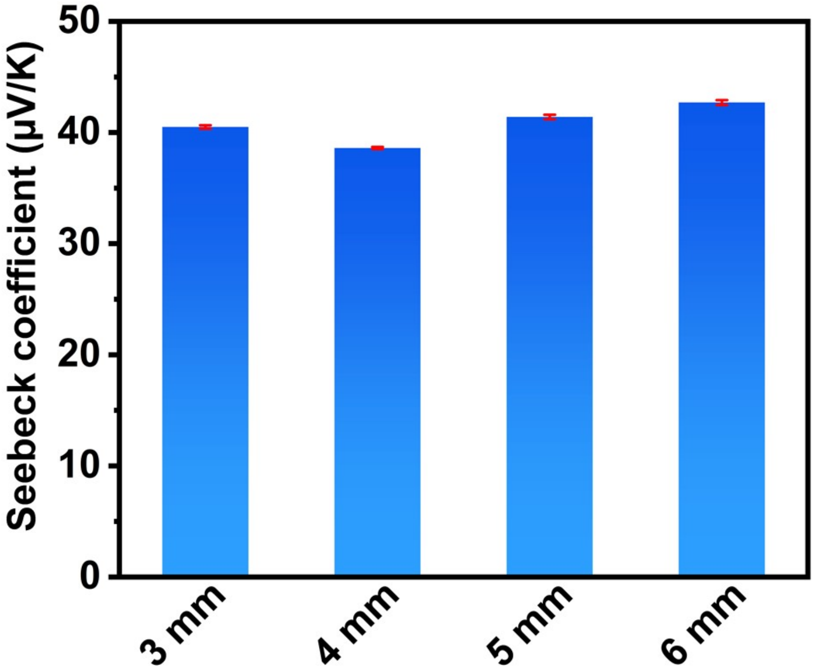

Figure S6. Seebeck coefficients of PCPP sensors with different thicknesses.

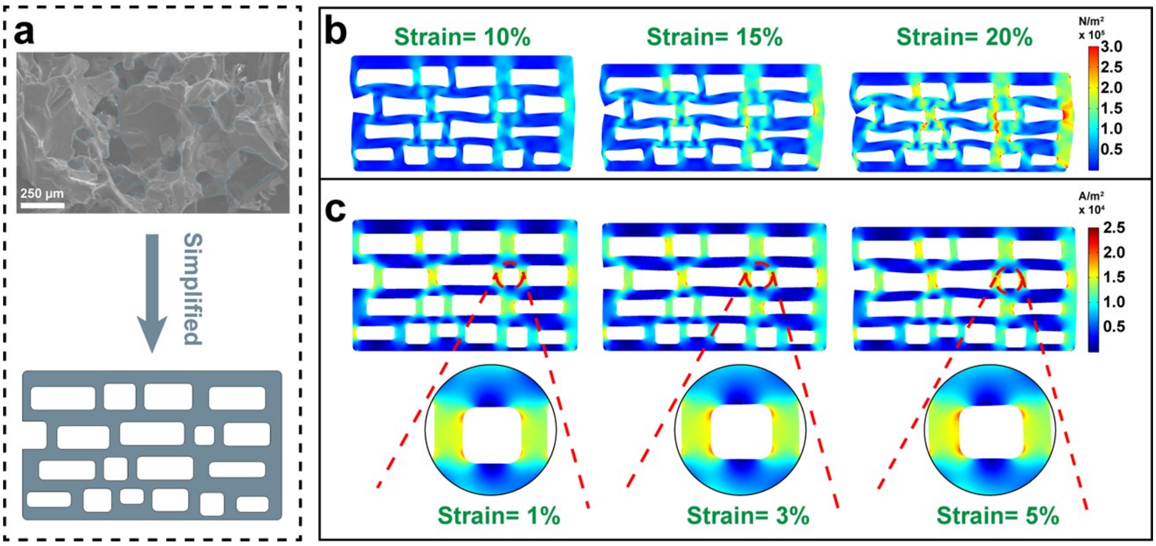

Figure S7. (a) SEM image and 2D simplification of a PCPP sensor structure. Simulation results on (b) stress distribution and (c) current density distribution of a PCPP sensor under different compressive strains.

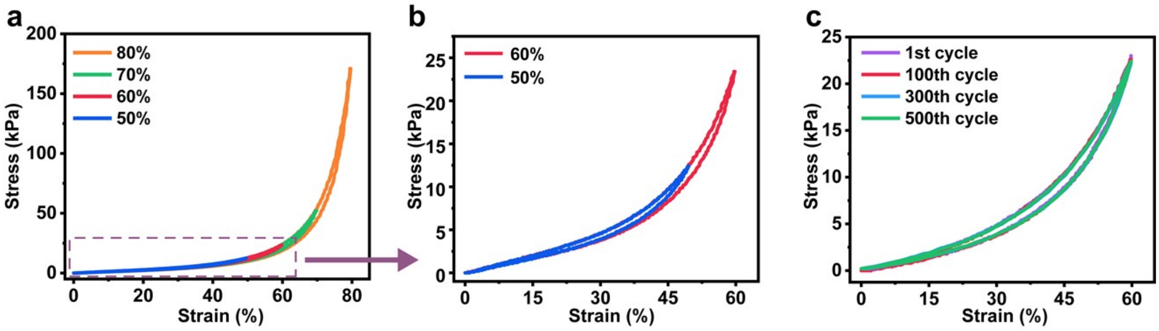

Figure S8. (a, b) Stress-strain curves of pure PDMS foam under different compressive strains (50%, 60%, 70%, 80%). (c) Cyclic compressive stress–strain curves of pure PDMS foam.

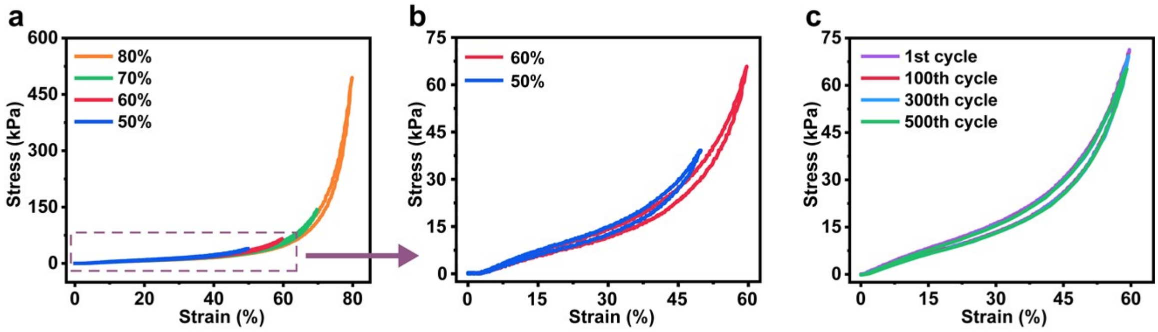

Figure S9. (a, b) Stress-strain curves of a PCPP foam under different compressive strains (50%, 60%, 70%, 80%). (c) Cyclic compressive stress–strain curves of the PCPP foam.

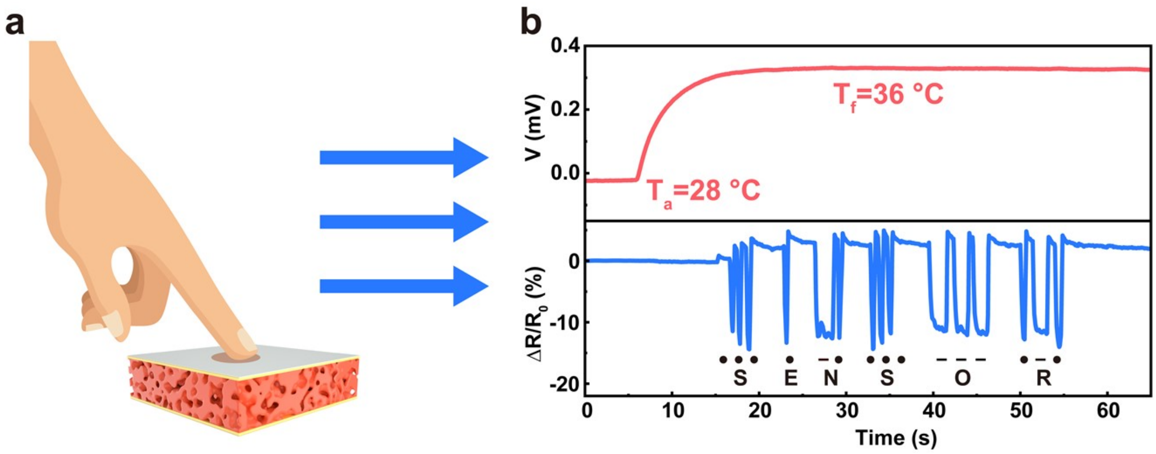

Figure S10. (a) A schematic diagram of regularly pressing the PCPP sensor with a finger, and (b) corresponding changes in both output voltage and $\Delta R/R_0$.

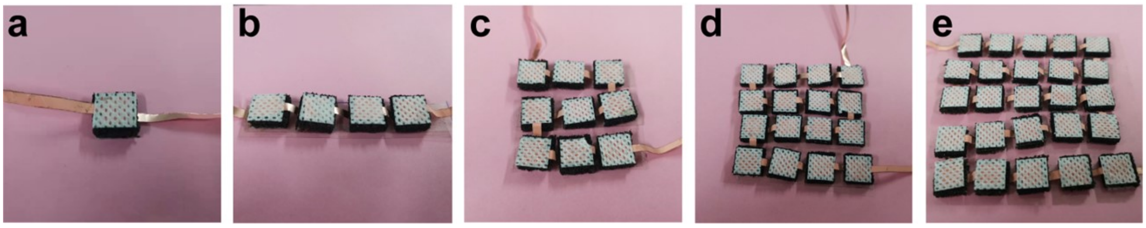

Figure S11. Digital photos of self-powered series-connected arrays: (a) Array-1; (b) Array-4; (c)Aarray-9; (d) Array-16; and (e) Array-25.

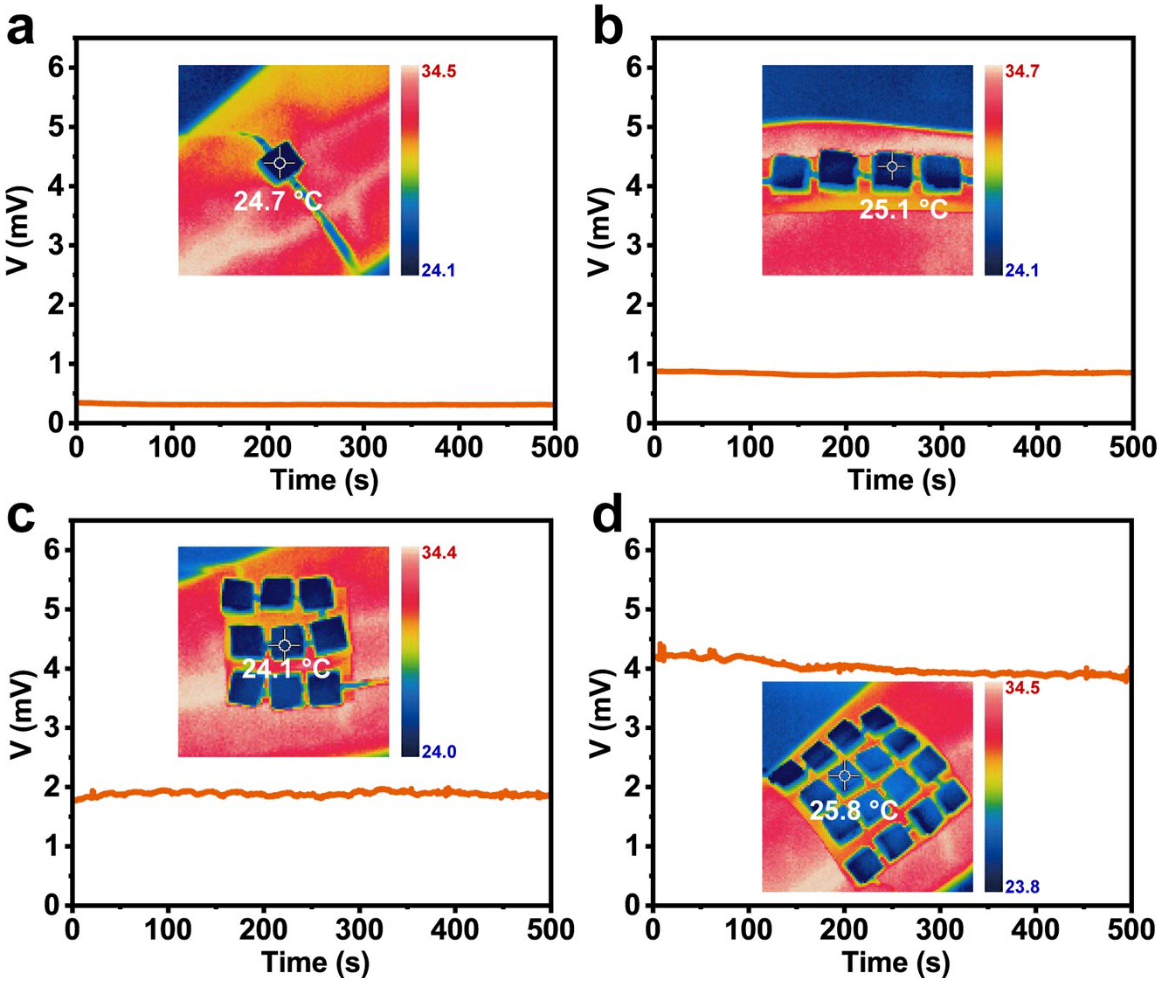

Figure S12. Output voltages of (a) Array-1, (b) Array-4, (c) Array-9, and (d) Array-16 covered by commercial hydrogels.

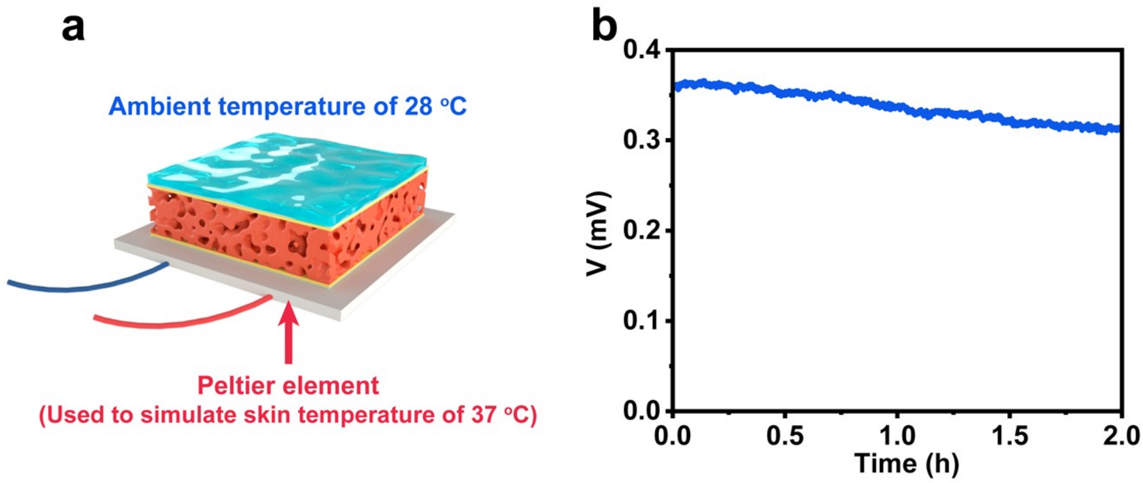

Figure S13. (a) The testing process and (b) the output voltages of the hydrogel-covered Array-1 within 2 h.

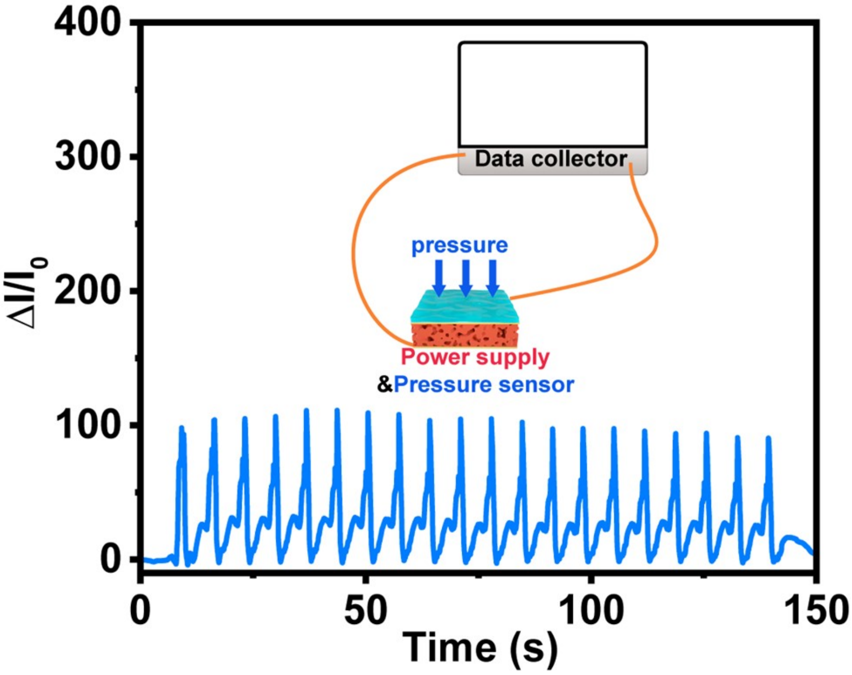

Figure S14. A single PCPP sensor detects external pressure without power driving (ΔT = ~10 K, pressure = 20 kPa)

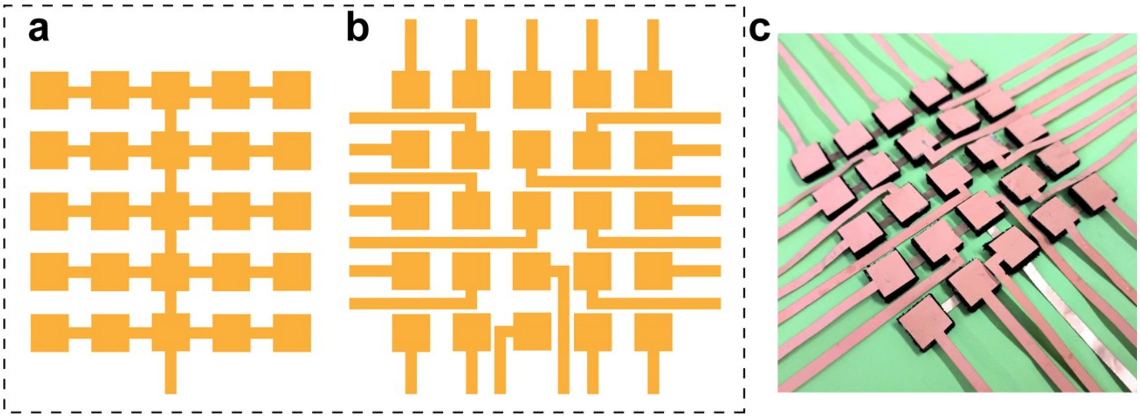

Figure S15. 5×5 E-skin array circuit diagram: (a) bottom surface electrode; (b) top surface electrode. (c) Optical photograph of a 5×5 E-skin array.

Multiphysics Field Simulation:

The stress distribution, current density distribution, and potential distribution of the PCPP sensor under different external stimuli were examined by the Multiphysics Field Simulation. The model is built by observing the microstructure of the PCPP based on its SEM images. Assuming that the PCPP is an isotropic linear elastic material, its deformation process under different strains can be described as follows:

$$0 = \boldsymbol{F_v} + \nabla\cdot S \tag{1}$$

$$S = S_{ex} + \boldsymbol{C}\boldsymbol{:}\varepsilon_{el} = S_{ex} + \boldsymbol{C}\boldsymbol{:}(\varepsilon\text{-}\varepsilon_{inel}) \tag{2}$$

$$\varepsilon = (1/2)[(\nabla\boldsymbol{u})^T + \nabla\boldsymbol{u}] \tag{3}$$

$$\boldsymbol{C} = \boldsymbol{C}(E,v) \tag{4}$$

Where $\boldsymbol{F_v}$ is the volume force, S is the stress, which is determined by the extra stress S_{ex} (e.g. initial stresses and viscoelastic stresses), the elastic matrix $\boldsymbol{C}$ (determined by the Young's modulus E and Poisson's ratio v of the material) and the elastic strain ε_{el} (the difference between the total strain ε and all inelastic strains ε_{inel}), $\boldsymbol{u}$ is the displacement.[11,12]

To obtain the current density distribution, we consider the whole system to be current conserving, and the process can be described as:

$$\boldsymbol{J} = \sigma\boldsymbol{E} + \boldsymbol{J_e} \tag{5}$$

$$\nabla\boldsymbol{J} = -\nabla\cdot(\sigma\nabla V - \boldsymbol{J_e}) = Q_j \tag{6}$$

$$\boldsymbol{E} = -\nabla V \tag{7}$$

Where $\boldsymbol{E}$ is the electric field intensity, $\boldsymbol{J}$ is the current density, σ is the electrical conductivity, and $\boldsymbol{J_e}$ is an externally generated current density.[13]

The heat transfer in the PCPP can be described as follows:

$$Q = \rho C_p \boldsymbol{u}\nabla T + \nabla\cdot\boldsymbol{q} \tag{8}$$

$$\boldsymbol{q} = -k\cdot\nabla T \tag{9}$$

Where Q contains additional heat sources, ρ is the density, C_p is the specific heat capacity at a constant stress, $\boldsymbol{u}$ is the velocity vector of the translational motion, $\boldsymbol{q}$ is the heat flux by conduction, k is the thermal conductivity.[14]

Thermoelectric effect is adopted to obtain potential distributions of the PCPP under different temperature differences and strains, which is described as follows:

$$-\nabla((\sigma S^2 T + \lambda)\nabla T) - \nabla(\sigma S T \nabla V) = \sigma((\nabla V)^2 + S\nabla T \nabla V) \tag{10}$$

$$\nabla(\sigma S\nabla T) + \nabla(\sigma\nabla V) = 0 \tag{11}$$

Where σ is the electrical conductivity, S is the Seebeck coefficient, and λ is the thermal conductivity.[15]

References

1. P. J. Taroni, G. Santagiuliana, K. N. Wan, P. Calado, M. T. Qiu, H. Zhang, N. M. Pugno, M. Palma, N. Stingelin-Stutzman, M. Heeney, O. Fenwick, M. Baxendale and E. Bilotti, *Adv. Funct. Mater.*, 2018, **28**, 1704285.

2. S. Han, N. U. H. Alvi, L. Granlof, H. Granberg, M. Berggren, S. Fabiano and X. Crispin, *Adv. Sci.*, 2019, **6**, 1802128.

3. M. Li, J. Chen, W. Zhong, M. Luo, W. Wang, X. Qing, Y. Lu, Q. Liu, K. Liu, Y. Wang and D. Wang, *ACS Sens.*, 2020, **5**, 2545-2554.

4. Y. Yang, G. Zhao, X. Cheng, H. Deng and Q. Fu, *ACS Appl. Mater. Interfaces*, 2021, **13**, 14599-14611.

5. F. Zhang, Y. Zang, D. Huang, C. A. Di and D. Zhu, *Nat. Commun.*, 2015, **6**, 8356.

6. S. Xu, Z. Fan, S. Yang, X. Zuo, Y. Guo, H. Chen and L. Pan, *ACS Sens.*, 2021, **6**, 1120-1128.

7. F. Li, Y. Liu, X. Shi, H. Li, C. Wang, Q. Zhang, R. Ma and J. Liang, *Nano Lett.*, 2020, **20**, 6176-6184.

8. X. He, Y. Hao, M. He, X. Qin, L. Wang and J. Yu, *ACS Appl. Mater. Interfaces*, 2021, **13**, 60498-60507.

9. Y. Wang, H. Mao, Y. Wang, P. Zhu, C. Liu and Y. Deng, *J. Mater. Chem. A.*, 2020, **8**, 15167-15176.

10. Y. Wang, H. Wu, L. Xu, H. Zhang, Y. Yang and Z. L. Wang, *Sci. Adv.*, 2020, **6**, eabb9083.

11. C. L. Choong, M. B. Shim, B. S. Lee, S. Jeon, D. S. Ko, T. H. Kang, J. Bae, S. H. Lee, K. E. Byun, J. Im, Y. J. Jeong, C. E. Park, J. J. Park and U. I. Chung, *Adv. Mater.*, 2014, **26**, 3451-3458.

12. Z. Wang, S. Wang, J. Zeng, X. Ren, A. J. Chee, B. Y. Yiu, W. C. Chung, Y. Yang, A. C. Yu, R. C. Roberts, A. C. Tsang, K. W. Chow and P. K. Chan, *Small*, 2016, **12**, 3827-3836.

13. R. Gupta, A. Kumar, S. Sadasivam, S. Walia, G. U. Kulkarni, T. S. Fisher and A. Marconnet, *ACS Appl. Mater. Interfaces*, 2017, **9**, 13703-13712.

14. L. Du, Z. Zhao, Z. Fang, Y. Feng and J. Yan, *IET Sci. Meas. Technol.*, 2017, **11**, 907-913.

15. I. M. Abdel-Motaleb and S. M. Qadri, *J. Electron. Cool. Therm. Control*, 2017, **07**, 123-135.